AIAA JOURNAL
Vol. 46, No. 10, October 2008

Modeling of Stardust Reentry Ablation Flows in the Near-Continuum Flight Regime

Jiaqiang Zhong,* Takashi Ozawa,* and Deborah A. Levin†
Pennsylvania State University, University Park, Pennsylvania 16802

DOI: 10.2514/1.36196

The ablation process of the Stardust thermal protection material is designed to reduce aerodynamic heating during reentry for extreme conditions. The coupling of ablation species with the flowfield is investigated in this work using the direct simulation Monte Carlo method for transitional to near-continuum flows. To model surface thermal and chemical ablation processes, a variable surface temperature wall is obtained assuming a radiative heat flux balanced by convective heat flux. It is found that chemical ablation due to the reaction between thermal protection system carbon materials and gaseous oxygen and nitrogen atoms is dominant compared with thermal ablation. As the altitude decreases, the forebody surface temperature increases, the ablation process becomes more intensive, and the influence of ionization reactions on the flowfield becomes more important due to denser freestream conditions.

Nomenclature

A	=	preexponential factor in rate coefficient expression
B	=	temperature exponent in rate coefficient expression
C_p	=	pressure coefficient
E_a	=	activation energy
e	=	electron charge, 1.6×10^{-19} C
f	=	frequency, Hz
f_p	=	plasma frequency, Hz
K_b	=	backward reaction rate constant
K_{eq}	=	equilibrium constant
K_f	=	reaction rate constant
k_B	=	Boltzmann constant
M	=	Mach number
m_e	=	mass of electron, 9.1×10^{31} kg
n_e	=	electron number density
P	=	reaction probability
Q	=	heat flux
T	=	temperature
T_e	=	electron temperature
T_{rot}	=	rotational temperature
T_{tr}	=	translational temperature
T_{vib}	=	vibrational temperature
T_w	=	wall temperature
U	=	speed
γ	=	specific heat ration
ϵ	=	surface emissivity
ϵ_0	=	permittivity 8.85×10^{12} F/m^2
ρ	=	density
σ	=	Stefan–Boltzmann constant, 5.67×10^{-8} W/(K^{4}m^2)

I. Introduction

THERMAL protection systems (TPS) are essential for the successful operation of space vehicles when they are subjected to intense aerodynamic heating during reentry processes [1]. Ablation, one of the most effective cooling processes, removes heat generated by the energetic flow to the vehicle surface by release of surface material. Because the loss of surface material is a one-way process and the amount of ablative material used affects the mass of the payload, it is important to accurately simulate ablation flows to support the more effective design of future spacecraft and the concept of aerobraking. Ablative TPS materials lose mass through multiple processes including chemical, thermal [2,3], and mechanical ablation [4].

Many studies on the modeling of spacecraft reentry ablation flow are available in the literature, so that we only mention a few relevant examples. Gosse and Candler [2] modeled the gas flow over a sphere–cone vehicle coupling in the solution of the mass and energy balance with surface reactions at an altitude of 16 km. In that work, the gas–surface reactions and surface sublimation were included, and it was found that the predicted surface recession rate for a validation case was lower than experimental measurements conducted in the U.S. Air Force Flight Dynamics Laboratory's 50-MW arc plasma generator and the Arnold Engineering Development Center's Aeroballistic Range. Suzuki et al. [3] conducted trajectory-based analyses using the computational fluid dynamics (CFD) method to model the aerodynamic heating environment for the MUSES-C superorbital reentry capsule. In their work, gas–surface oxidization and nitridation and surface sublimation ablation at altitudes of 49–81 km was studied, and it was shown that the wall temperature in the downstream region is significantly elevated by the turbulence effect caused by gaseous ablation products. Chen and Milos [5] studied a hypersonic flowfield over a dense carbon–phenolic heat shield under flow conditions typical for earth reentry from a planetary mission. The ablation surface boundary conditions of oxidation, nitridation, and material sublimation were coupled with a Navier–Stokes solver, and it was found that the surface ablation had only a small impact on the predicted convective heat flux.

A number of TPS ablation studies have been performed for Stardust reentries. The Stardust sample return capsule [6] was protected by a low-density heat-shield material known as phenolic impregnated carbon ablator (PICA) during its reentry of about 12 km/s, the fastest man-made reentry to date. The PICA material has a mass fraction of 92% carbon, 4.9% oxygen, 2.2% hydrogen, and 0.9% nitrogen. Covington et al. [1] conducted arcjet tests to study the ablative and thermal performance of the PICA material. The arcjet tests were conducted to simulate the peak heating conditions expected during the Stardust entry process. It was found that the maximum surface temperature on the PICA thermal protection layer is about 3000 K, the heating rate is about 1630 W/cm^2, and the ablation recession rate is in the range of 7–9 cm/s. Wilmoth et al. [7] studied Stardust aerodynamics in the transitional region using direct simulation Monte Carlo (DSMC), Navier–Stokes, and Newtonian methods, and it was found that the

Presented as Paper 4551 at the 39th AIAA Thermophysics Conference, Miami, FL, 25–28 June 2007; received 13 December 2007; revision received 18 April 2008; accepted for publication 7 May 2008.

*Postdoctoral Research Fellow, Department of Aerospace Engineering. Member AIAA.

†Professor, Department of Aerospace Engineering. Associate Fellow AIAA.

axial and normal forces and the pitching moment agreed reasonably well among the various methods. Olynick et al. [8] modeled Stardust entry flows with coupled radiation and ablation by solving the axisymmetric nonequilibrium Navier–Stokes equations loosely coupled with a radiation and a material thermal response models. It was shown [8] that the Stardust surface ablation rate increases as the surface heat flux rate increases, the dominant ablation species are C and CO, and the peak ablation rate on the forebody stagnation point is about 0.01–0.09 kg/(m^2 s) at altitudes between 45–81 km. Assuming a fully thermal and chemical equilibrium flowfield, Gupta [9] applied an axisymmetric viscous shock layer method and coupled radiation solutions with and without chemical and thermal ablation for Stardust reentry flows at altitudes of 46–81 km. It was found that the ablation model with a rate of about 0.04 kg/(m^2 s), similar to [8], predicted a decrease of the maximum stagnation heating by about 35% compared with the nonablation simulation result.

For high-energy reentry flows such as Stardust, ionization processes cannot be neglected, even at high altitudes. The presence of charged species potentially affects the overall flowfield features and, more important, charged species cause blackout communication problems [10,11]. Generally, the communication antennas are located on the aft body, so that the prediction of electron number density in the wake is important. Morabito [12] discussed the blackout for the Mars Science Laboratory (MSL) and Apollo Earth reentries and compared CFD results with observations. Starkey [10] investigated blackout problems for the RAM-C II and space shuttle vehicles.

In this work we will study the Stardust reacting thermal and chemical ablation flows at 81- and 68.9-km altitudes. It is well known that the flowfield at this altitude is in the rarefied and transitional regions [13,14], so that the continuum assumption is not accurate any more. We choose the particle-based DSMC method to model axisymmetric Stardust reentry ablation flows at altitudes of 68.9 and 81 km because the actual angles of attack at the simulated altitudes are close to zero [7]. This work represents the first modeling of chemical ablation including ionization processes in the non-continuum flight regime. Before this work, the aforementioned phenomena have been considered primarily during peak heating. The simulation results presented in this work were obtained from the modified DSMC SMILE code [15]. The paper is organized as follows: freestream flow surface boundary conditions are given in Sec. II, and the reacting thermal and chemical ablation models are described in Sec. III. In Sec. IV, the modeling of ionization processes and charged species in DSMC are presented. An iterative method is applied in Sec. V to obtain an accurate Stardust surface temperature distribution based on a thermal equilibrium condition between the gas convective heating and surface radiation cooling, and the impact of surface temperature on flowfield and surface parameters are further discussed. The structure of the reacting thermal and chemical ablation flow and the surface result sensitivity to altitude are discussed in Sec. VI. because ionization processes and charged species are included in the DSMC calculations, the communication blackout problem may be assessed as is discussed in Sec. VI. Conclusions are summarized in Sec. VII.

II. Flow Conditions and Geometry

The Stardust geometry is modeled as a 60-deg half-angle blunt body with a nose radius of about 0.23 m, as shown in Fig. 1. Note that the symbol S in this work refers to the surface distance starting from the forebody stagnation point. The freestream conditions for the two Stardust reentry flows considered in this work, at 68.9 and 81 km, are listed in Table 1. These two freestream conditions were chosen because they correspond to conditions of transitional to near-continuum flow. In our DSMC simulations, the variable hard sphere model is used to simulate neutral species collisions, and the Borgnakke–Larsen model is applied to distribute postcollisional energy between kinetic and internal modes. In our previous modeling [13], a constant surface temperature was assumed in our reentry flow simulations, but in this paper our focus is on the gas–surface

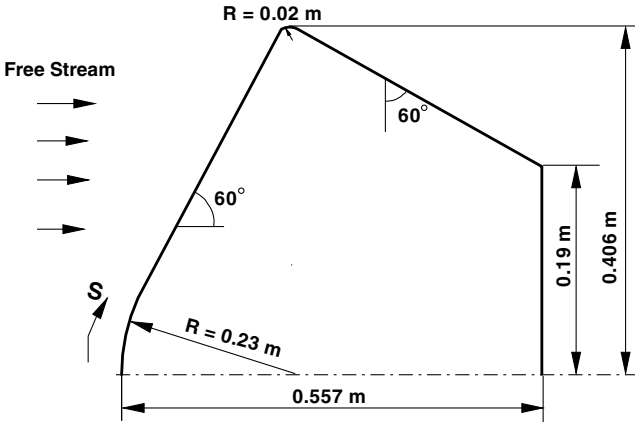

Fig. 1 Stardust geometric configuration.

interactions. The constant surface temperature assumption is not sufficiently accurate for modeling the Stardust gas–surface processes, which are closely related to the incident heat flux. We will apply an iterative method to obtain a more realistic surface temperature distribution based on the assumption of equilibrium between thermal heating and radiation cooling. To further study the impact of surface temperature on the ablation process, we will compare the simulation results obtained with the variable surface temperature distribution with a constant temperature wall condition of 2038 K, approximately the average value of the forebody surface temperature. In this work, a diffuse wall boundary condition is assumed with full thermal accommodation, i.e., the thermal and chemical ablated gaseous species released from the wall surface during the simulation are also assumed to have full thermal accommodation with the wall.

III. Chemical Reaction and Ablation Models

Two kinds of ablation mechanisms, thermal and chemical, are studied in this work. Thermal ablation is due to environmental heating of the TPS leading to TPS material melting and evaporation. Chemical ablation is due to the bow-shock gaseous species chemical reactions with the thermal protection char layer, leading to the release of gaseous reaction products.

To study the Stardust reentry chemically reacting thermal and chemical ablation flow, we compared four simulation cases in this work, nonreacting flow, chemically reacting flow, chemically reacting with thermal ablation flow, and chemically reacting with thermal and chemical ablation flow. Table 2 lists the chemical reactions and chemical rates modeled in the flow for 15 dissociation and 4 exchange reactions for five oxygen- and nitrogen-derived chemical species [16]. When thermal ablation is modeled, it is assumed in this work that there is a constant thermal ablation rate from the forebody surface as given in Table 1 with a mass fraction of

Table 1 Freestream conditions and thermal ablation rates for the two altitudes considered in this work

	68.9 km	81 km
	Freestream	
Velocity, km/s	11.900	12.391
Mach number	39.65	41.87
Temperature, K	224.0	217.60
Number density, mole/m^{-3}	1.6023×10^{21}	2.6388×10^{20}
N_2 mole fraction	76.28%	76.23%
O_2 mole fraction	23.72%	23.72%
Knudsen number	1.89×10^{-3}	1.28×10^{-2}
	Thermal ablation characteristics	
Rate, kg/(m^{2}s)	4.0×10^{-02}	1.6×10^{-02}
C mass fraction	60%	60%
CO mass fraction	40%	40%

Table 2 List of chemical reactions for air species [16]. Note that E_a is the reaction activation energy, A and B are the constants in the Arrhenius reaction rate equation $k_f = AT^{-B}\exp(-E_a/kT)$

No.	Reaction	Enthalpy, $\times 10^{-19}$ J	A	B	E_a, $\times 10^{-19}$ J
1	$O_2 + N \rightarrow O + O + N$	8.197	5.593×10^{-12}	1.0	8.197
2	$O_2 + NO \rightarrow O + O + NO$	8.197	5.593×10^{-12}	1.0	8.197
3	$O_2 + N_2 \rightarrow N_2 + O + O$	8.197	1.193×10^{-11}	1.0	8.197
4	$O_2 + O_2 \rightarrow O_2 + O + O$	8.197	5.393×10^{-11}	1.0	8.197
5	$O_2 + O \rightarrow O + O + O$	8.197	1.498×10^{-10}	1.0	8.197
6	$N_2 + O \rightarrow O + N + N$	15.61	3.187×10^{-13}	0.5	15.61
7	$N_2 + O_2 \rightarrow O_2 + N + N$	15.61	3.187×10^{-13}	0.5	15.61
8	$N_2 + NO \rightarrow NO + N + N$	15.61	3.187×10^{-13}	0.5	15.61
9	$N_2 + N_2 \rightarrow N_2 + N + N$	15.61	7.968×10^{-13}	0.5	15.61
10	$N_2 + N \rightarrow N + N + N$	15.61	6.900×10^{-8}	1.5	15.61
11	$NO + N_2 \rightarrow N + O + N_2$	10.43	6.590×10^{-10}	1.5	10.43
12	$NO + O_2 \rightarrow N + O + O_2$	10.43	6.590×10^{-10}	1.5	10.43
13	$NO + NO \rightarrow N + O + O_2$	10.43	1.318×10^{-8}	1.5	10.43
14	$NO + O \rightarrow N + O + O$	10.43	1.318×10^{-8}	1.5	10.43
15	$NO + N \rightarrow N + O + N$	10.43	1.318×10^{-8}	1.5	10.43
16	$NO + O \rightarrow O_2 + N$	2.719	5.279×10^{-21}	−1	2.719
17	$N_2 + O \rightarrow NO + N$	5.175	1.120×10^{-16}	0	5.175
18	$O_2 + N \rightarrow NO + O$	−2.719	1.598×10^{-18}	−0.5	0.4968
19	$NO + N \rightarrow N_2 + O$	−5.175	2.490×10^{-17}	0	0

60% carbon and 40% CO molecules, taken from the work of Olynick et al. [8] In the DSMC calculation a source of simulated particles composed of C and CO at the preceding flux rate is introduced into the computational domain per time step. Note that the thermal ablation rate on the afterbody surface is assumed to be zero because the gas–surface heat flux is negligible on the afterbody compared with the forebody surface. The ablated molecules are assumed to be in a state of full thermal accommodation with the wall. For the chemical ablation model, it is assumed that as flowfield nitrogen and oxygen atoms collide with the thermal protection carbon wall, surface oxidation and nitridation occurs as

$$\mathrm{O} + \mathrm{C}(s) \rightarrow \mathrm{CO} \tag{1}$$

and

$$\mathrm{N} + \mathrm{C}(s) \rightarrow \mathrm{CN} \tag{2}$$

The carbon surface oxidation shown in Eq. (1) has a reaction probability [2,3] of $P_o = 0.63\exp(-1160/T_w)$, where T_w is the wall temperature. The carbon surface nitridation probability, as shown in Eq. (2), is assumed to be 1.0 independent of the wall temperature, as implemented in the work of Suzuki et al. [3] Again, the gaseous chemical ablation products CO and CN are assumed to be fully thermally accommodated with the wall.

Because the gaseous CN species strongly radiates [17], accurate prediction of the CN species spatial distribution is critical if one is to compare the simulated radiation intensity with measured spectral data, which may be available in the future. In addition to carbon surface ablation, another potential source of CN radiation may be that generated from the dissociation and exchange reactions of small amounts of CO_2 (with a mole fraction of about 0.1%) existing in the atmosphere. Such radiation from the CN species was detected in the noncatalytic Planetary Atmosphere Experiments Test (PAET) vehicle reentry flow [18]. The dissociation and exchange reactions related to carbon species [19] are listed in Table 3, where the symbols A and M represent any type of atom and molecule, respectively, from the list of species. To study the importance of freestream contributions to the reentry flow CN number density, we added a mole fraction of 0.1% CO_2 to the freestream flow conditions at 81 km, given in Table 1, and conducted a nonablation reacting flow simulation using a constant wall temperature of 2730 K. The species CO, CN, and CO_2 number densities obtained from the steady-state flow solution along the forebody stagnation line are shown in Fig. 2. Note that the additional 0.1% CO_2 in the freestream had no other detectable impact on the flowfield and surface macroparameters. It can be seen that there is a small amount of CO and CN existing in the nonablation flow, generated from CO_2 dissociation and CO exchange reactions. It will be shown in Sec. VI that the CO and CN number densities obtained from simulations that include thermal and chemical ablation flow are about 2–5 orders of magnitude larger than the values in the nonablation flow. Therefore, the freestream CO_2 contribution to the formation of CO and CN is negligible in the chemically reacting thermal and chemical ablation flow and is not considered further in this work.

IV. Modeling of Ionization

The most widely used chemical reaction model in DSMC is the total collision energy (TCE) model [20,21]. In our work, ionization processes are treated as chemical reactions; therefore, the TCE model is used to model these processes as well. In the TCE model, the reaction probability has a form that allows one to match reaction rates $K_f(T)$ obtained from experiments

$$K_f = AT^{-B}\exp\left(-\frac{E_a}{k_B T}\right) \tag{3}$$

The ionization processes that will be considered in the flow modeling are taken from [22] and are listed in Table 4. For electron impact ionization reactions, such as $e^- + \mathrm{N} \rightarrow e^- + \mathrm{N}^+ + e^-$ and $e^- + \mathrm{O} \rightarrow e^- + \mathrm{O}^+ + e^-$, to be used in the TCE model, the Arrhenius parameters are modified for the required high-temperature range. The modified rates were found to agree well with the original reaction rates of Park [22]. The chemical process $\mathrm{N} + \mathrm{O} \rightarrow$

Table 3 List of carbon species chemical reactions [19], where A and M represent any type of atom and molecule

No.	Reaction	Enthalpy, $\times 10^{-19}$ J	A	B	E_a, $\times 10^{-19}$ J
1	$CO_2 + A \rightarrow CO + O + A$	8.732	2.325×10^{-8}	1.5	8.732
2	$CO_2 + M \rightarrow CO + O + M$	8.732	1.146×10^{-8}	1.5	8.732
3	$CO + M \rightarrow C + O + M$	17.80	5.650×10^{-10}	1.0	17.80
4	$CN + M \rightarrow C + N + M$	9.80	4.150×10^{-16}	1.0	9.80
5	$CO + N \rightarrow CN + O$	5.327	1.661×10^{-16}	0.0	5.327
6	$C + N_2 \rightarrow CN + N$	3.202	1.827×10^{-16}	0.11	3.202

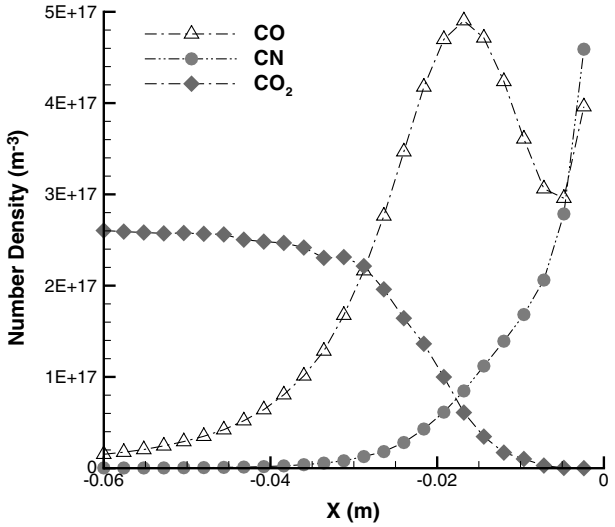

Fig. 2 Species CO, CN, and CO_2 number density along the forebody stagnation line with 0.1% CO_2 mole faction at freestream at 81 km.

$NO^+ + e^-$ is the initiating ionization process, and $e^- + N \rightarrow e^- + N^+ + e^-$ has the highest ionization rate at high temperatures.

The backward rates are computed from an equilibrium constant, $K_b = K_f/K_{eq}$, where K_b is the backward rate, K_f is the forward rate, and K_{eq} is the equilibrium constant for the reaction. The preferred method of computing equilibrium constants is to use the minimized Gibb's free energy method, where species enthalpy and entropy are computed using curve-fit expressions given by Gordon and McBride [23] and the equilibrium constant is then determined via the van Hoff't equation. The backward rates K_b obtained from equilibrium constants are finally refitted into an Arrhenius form based on the temperature dependence of the equilibrium constant. Arrhenius rate parameters were obtained for recombination rates and are listed in Table 4.

The modeling of ionization flow is challenging in DSMC because the electron mass is approximately 5 orders of magnitude lighter and the thermal velocity is approximately 2 orders of magnitude higher than the neutral air species. The Debye length for the Stardust flowfields between 68.9 and 81 km is much smaller than local mean free path, therefore charge neutrality must hold in the flowfield. For these reasons, a single-time step method was used in this work to maintain charge neutrality in the DSMC simulation by moving electrons based on the local average ion velocity [24]. The DSMC-based SMILE [15,25] code was modified to accommodate charged particles, and further details may be found in [13].

V. Modeling of Stardust Surface Properties and Effect on Flowfield

A. Surface Temperature Distributions

Most of the available work in the literature assumes a spatially uniform constant surface temperature for spacecraft reentry flow simulations [26,27]. However, this assumption is not accurate because the surface temperature is closely related to heat flux, and due to the high-temperature bow shock, the heat flux on the forebody is much greater than on the afterbody. Therefore, the forebody surface temperature should be larger than the afterbody surface temperature. Because the surface temperature impacts the Stardust reacting thermal and chemical ablation flowfield, it is important to use an accurate surface temperature distribution in the simulation, as will be shown in this section.

In this work, we apply an iterative method to obtain an accurate surface temperature distribution based on the assumption of a thermal equilibrium condition between the gaseous thermal heating and body radiation cooling as follows [8,9,28]:

$$Q = \epsilon \sigma T_w^4 \tag{4}$$

where Q is the gaseous heat flux to the wall obtained from the DSMC simulation, ϵ is the Stardust surface emissivity assumed to be 0.9, and σ is the Stefan–Boltzmann constant, and T_w is the wall temperature. Note that the emissivity value of 0.9 was originally recommended by Covington et al. [1] and is consistent with the value measured for PICA and other carbonaceous ablators [29]. In the iterative simulations, we assume an initially, spatially uniform surface temperature of 2730 K, which is the average forebody temperature for the nonreacting case at 81 km, to obtain a surface heat flux distribution from the DSMC simulation. Then using Eq. (4), we obtain a new surface temperature distribution, which is reapplied to the second DSMC calculation. This procedure is repeated until the heat flux and surface temperature from two consecutive calculations are converged. The entire Stardust surface is divided into 56 panel elements in order to accurately sample the spatial variation of the surface heat flux in the DSMC calculation.

The iterative axisymmetric DSMC reacting thermal and chemical ablation simulation results of the Stardust surface heat fluxes and temperatures are shown in the Fig. 3 for an initial constant surface temperature of 2730 K. Radial weighting factors are used in the axisymmetric DSMC simulations to reduce the number of simulated particles. It can be seen that the surface heat flux and temperature are converged quite well after three iterations, suggesting that the surface may be modeled using a thermal equilibrium condition for the converged surface temperature for the transitional flow at 81 km. In a similar manner, we can obtain Stardust surface temperature distributions for nonreacting, reacting, and reacting thermal ablation flow, as shown in Fig. 4. It can be seen that for the entire body the nonreacting flow surface temperature is about 500 K higher than for the reacting flows because the gas temperature in the reacting flow is lower than the nonreacting flow due to energy consumption during the molecular dissociation processes. Because there is not much difference in the spatial distribution of the surface temperature between the reacting and reacting thermal ablation flow, it may be concluded that thermal ablation is not the dominant surface cooling process for these conditions. Figure 4 also shows that reacting, chemical-ablation reduces the forebody temperature by about 500 K compared with reacting, thermal ablation flow. However, when the reacting flow reaches the wake, it is further rarefied such that all three

Table 4 Ionization reactions used in the TCE model[a]

Reaction	A, m^3/s	B	E_a, $\times 10^{19}$ J	Reference
(1) $N + O \rightarrow NO^+ + e^-$	8.80×10^{-18}	0.000	4.40	Park [22]
(2) $N + N \rightarrow N_2^+ + e^-$	3.39×10^{-17}	0.000	9.32	Park [22]
(3) $O + O \rightarrow O_2^+ + e^-$	1.83×10^{-17}	0.000	11.1	Park [22]
(4) $e^- + N \rightarrow e^- + N^+ + e^-$	4.15×10^{3}	−3.82	23.3	Park [22]
(4) $e^- + N \rightarrow e^- + N^+ + e^-$	9.00×10^{-11}	−1.00	15.0	Modified
(5) $e^- + O \rightarrow e^- + O^+ + e^-$	6.48×10^{3}	−3.78	21.9	Park [22]
(5) $e^- + O \rightarrow e^- + O^+ + e^-$	3.00×10^{-10}	−1.00	14.0	Modified
(1R) $NO^+ + e^- \rightarrow N + O$	2.00×10^{-6}	−2.05	0.00	
(2R) $N_2^+ + e^- \rightarrow N + N$	1.00×10^{-8}	−1.43	0.00	
(3R) $O_2^+ + e^- \rightarrow O + O$	6.00×10^{-8}	−1.60	0.00	

[a]See Eq. (3).

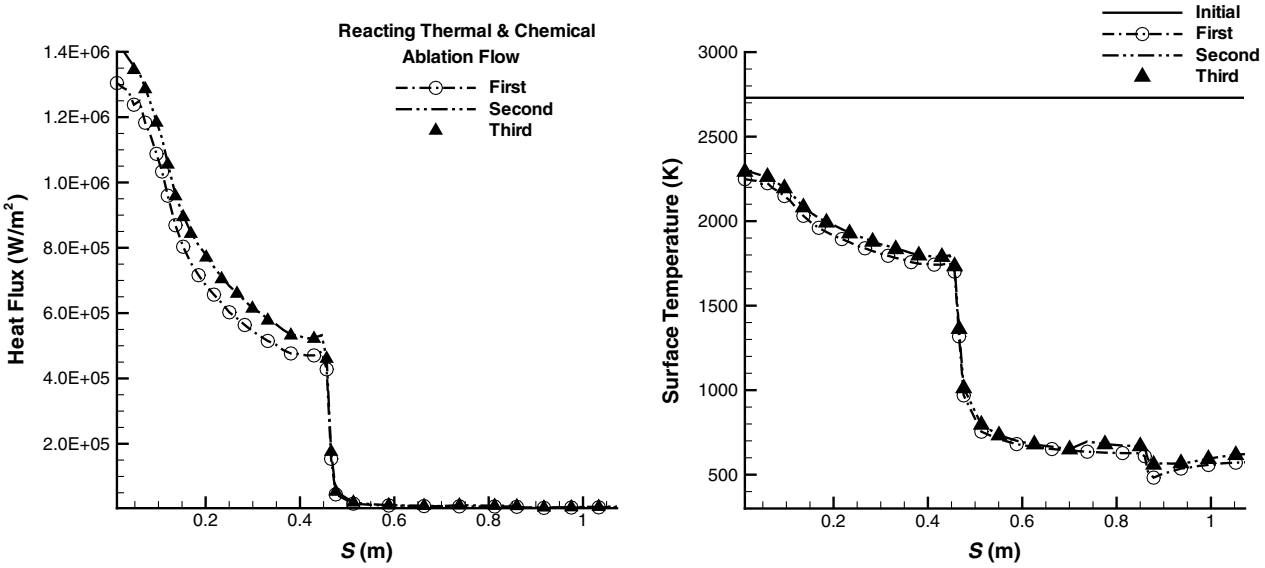

Fig. 3 Iterative DSMC reacting thermal and chemical ablation simulation results of Stardust surface heat flux (left) and temperature. In this work, S refers to the surface distance starting from the forebody stagnation point. A value of $S = 0.44$ m corresponds to the shoulder of the vehicle.

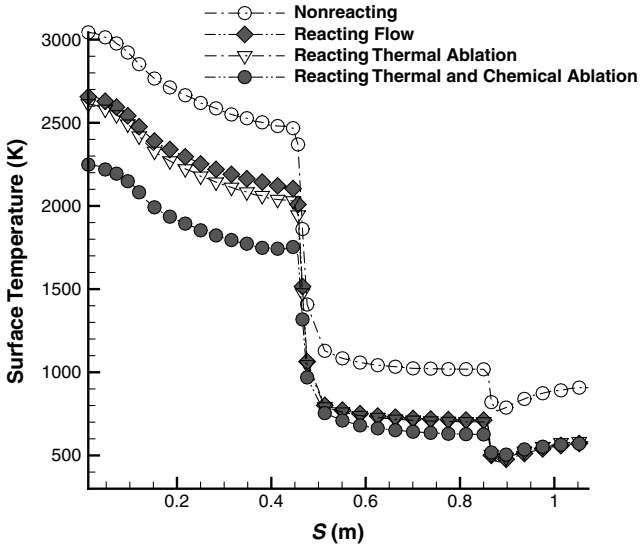

Fig. 4 Stardust surface temperature distributions for nonreacting, reacting, reacting thermal ablation, and reacting thermal and chemical ablation flows. The symbol S in this work refers to the surface distance starting from the forebody stagnation point.

predicted afterbody surface temperatures are essentially the same. Thus, chemical ablation is the dominant cooling process for Stardust transitional forebody reentry flow.

B. Surface Temperature Effect on Flowfield

To quantify the impact of variable surface temperature, we compared the reentry reacting thermal and chemical ablation flows at 81 km using a variable and constant temperature surface boundary condition. The variable temperatures are the converged temperature distribution as shown in Fig. 3, and the constant temperature surface has a value of 2038 K, which is approximately the average value of the variable forebody surface temperature. The simulation results showed that there was no observable difference of the forebody stagnation line flow parameters obtained for the condition of the variable or constant surface temperatures. This is because the assumed constant surface temperature 2038 K is close to the variable temperature on the forebody surface with a deviation of about 200 K, which has limited impact on the forebody flowfield as well as the forebody heat flux. Although the constant temperature 2038 K is much higher than the afterbody variable temperature, it is interesting to note that the constant surface temperature also has negligible impact on the afterbody surface heat flux because its value is quite small due to the rarefied conditions in the wake flow.

However, the surface temperature variation can impact the afterbody flowfield spatial distributions of species concentration because the surface oxidation reaction probability depends on the surface temperature. As Figs. 3 and 4 show, the variable afterbody surface temperature is much less than the constant value (2038 K). It is easier to detect the impact of variable surface temperature on the afterbody flow region because the ablation products move in the same direction as the flow velocity in the wake region. Figure 5 compares species number density along the wake afterbody stagnation line for reacting thermal and chemical ablation flow predictions for variable and constant surface temperatures. It can be seen from Fig. 5 that the atomic O concentration in the near wake region is much higher for the simulation that employs a variable wall temperature, although the sensitivity of the other species number densities to surface temperature is not significant. The main reason is that the higher afterbody surface temperature corresponds to a higher oxidation ablation probability, which consumes more atomic oxygen in the wake flow region. Note that, as mentioned earlier, the nitridation ablation probability is assumed to be unity in this work [3]. Therefore, the afterbody surface temperature will have a significant impact on the wake atomic O and N concentrations. The concentrations of the C, CO, and CN ablation products in the afterbody wake region are quite close for the two surface temperature models because these chemical species are mainly created in the forebody bow-shock region and then convected back to wake. The slight difference of these ablation product concentrations in the wake region occurs because as the afterbody surface temperature decreases, the reflected and ablated molecules from the wall have a lower thermal velocity leading to a longer molecular residence time, and, therefore, a larger number flux at the wall.

C. Prediction of Surface Parameters

To complete the discussion of the prediction surface properties for transitional hypersonic flows, we present the modeling of surface heat flux, surface pressure, and shear stress coefficients. Figure 6 compares the predicted heat flux, surface pressure, and shear stress for the Stardust nonreacting, reacting, thermal ablation, and thermal and chemical ablation flows. The nondimensional heat flux, surface pressure, and shear stress coefficients are normalized to the value of $\rho_\infty U_\infty^3/2$, $\rho_\infty U_\infty^2/2$, and $\rho_\infty U_\infty^2/2$, respectively. It can be seen that the surface parameters on the forebody are significantly higher than

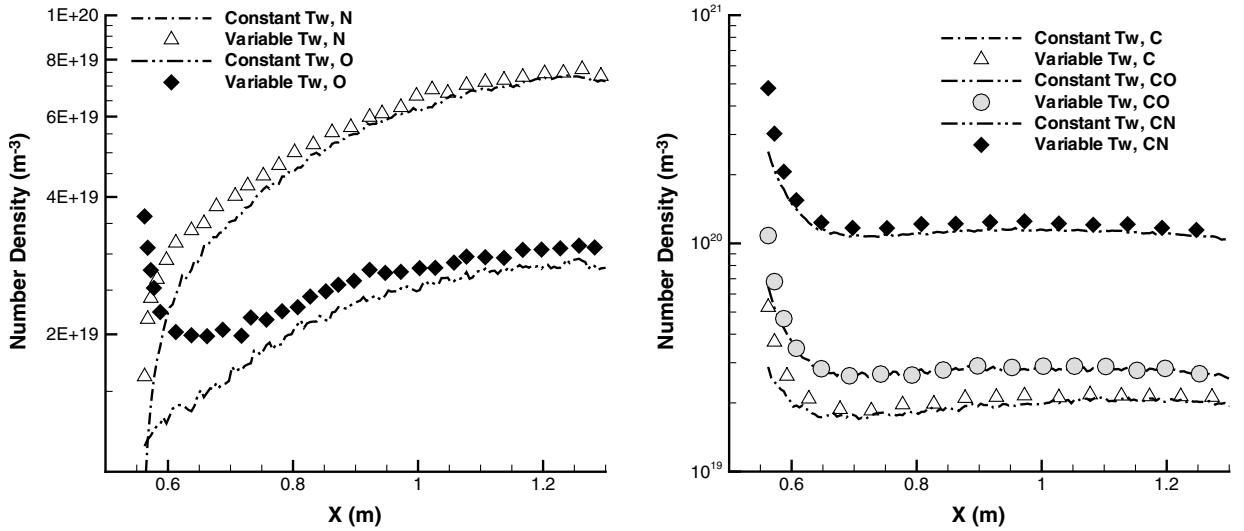

Fig. 5 Comparison of species number density along the afterbody stagnation lines in the reacting thermal and chemical ablation flow between simulations using variable and constant surface temperatures. The base of the vehicle is located at $x = 0.557$ m.

the values on the afterbody surface, suggesting that even in transitional flows the forebody and afterbody thermal protection layer design requirements are different. Although thermal and chemical ablation has no observable impact on the surface pressure, they effectively decrease the heat flux on the forebody surface. The DSMC-computed heat fluxes that were used to obtain the surface temperature profiles presented earlier in Fig. 4 are shown in the top portion of Fig. 6. The figure shows that the maximum heat flux coefficient on the forebody stagnation point decreases approximately from 0.36 obtained from the nonreacting flow to 0.21 and 0.1 when chemically reacting, thermal ablation, and chemical ablation processes are considered. Compared with thermal ablation, chemical ablation is seen to be a more effective mechanism that contributes to the Stardust surface cooling during the early portion of the reentry. As shown in the bottom figure of Fig. 6, the surface shear stress, which indicates the resistance of the surface to the peeling of carbon material from the thermal protection layer, is also impacted to some extent by the reacting and ablation models. Because the maximum surface shear stress on the shoulder is less than 250 Pa, at least 4 orders of magnitude less than the material critical value [4], the mechanical ablation process can be neglected during the early portion of the Stardust reentry.

Zhong et al. [30] provide a comparison of the predicted surface parameters presented in this work with those of Bird [20] and Moss et al. [31] using the DS2V code at an altitude of 81 km. For a chemical model of five species and 19 air chemical reactions, good agreement was found between the flow and surface parameters predicted by these two independent DSMC simulation codes. The present numerical surface heat flux and pressure for the chemical reaction flow are now compared with a semi-empirical equation and theoretical expression as follows.

A general semi-empirical equation was obtained for the convective aerodynamics heating on the entry spacecraft forebody stagnation point as [32,33]

$$Q = (1.76 \times 10^{-4} \rho_\infty^{0.5} V_\infty^3)/\sqrt{R_e} \tag{5}$$

where V_∞ is the freestream velocity in units of meters/second, ρ_∞ is the freestream mass density in units of kg/m^3, R_e is the radius of the surface stagnation point in units of m, and the convective heating flux Q is in units of W/cm^2. The heating rate predicted by Eq. (5) was found to have excellent agreement with the Fire II data as discussed in [32] and more recently reverified in ground Earth reentry high-enthalpy test measurements [34]. As shown in Fig. 6, the Stardust convective heating at 81 km for the chemically reacting case at the forebody stagnation point has a value of about 250 W/cm^2 from the DSMC calculation, which is very close to the value of 248.3 W/cm^2 predicted from Eq. (5). Therefore, we may conclude that our DSMC model can accurately predict surface heat flux as compared with the semi-empirical result of Eq. (5). Although the Stardust forebody surface has convective heating flux more than three times larger than the space shuttle reentry heating rate of about 80 W/cm^2 [35], the chemical ablation process can effectively protect Stardust from such high aerodynamic heating flux through significantly decreasing the heat flux to about 139 W/cm^2 at the forebody stagnation point.

Figure 6 shows a comparison of the surface pressure coefficients to the theoretical predictions from Newtonian theory. Based on Newtonian theory, surface pressure coefficient C_p can be approximately written as [36]

$$C_p = C_{p,\max} \cos^2\theta \tag{6}$$

where θ is the angle between the freestream velocity and the body surface. The maximum value of the pressure coefficient, $C_{p,\max}$, is given in normal shock wave theory as

$$C_{p,\max} = \frac{2}{\gamma M_\infty^2}\left\{\left[\frac{(\gamma+1)^2 M_\infty^2}{4\gamma M_\infty^2 - 2(\gamma-1)}\right]^{\gamma/(\gamma-1)}\left[\frac{1-\gamma+2\gamma M_\infty^2}{\gamma+1}\right] - 1\right\} \tag{7}$$

where M_∞ is the freestream Mach number, and γ is the specific heat ratio with a value of 1.286 for the air species [36]. It can be seen from Fig. 6 that the numerical prediction of the surface pressure coefficient agrees well with the Newtonian theory in the region close to the stagnation point. Because $C_{p,\max}$ in Eq. (7) is derived from normal shock wave theory, it cannot accurately predict the surface pressure at locations far from the forebody stagnation point where the gas experiences an oblique shock compression process.

VI. Forebody and Wake Flowfield Results

The freestream conditions, reacting ablation models, variable surface temperatures, and ionization models discussed in the preceding sections will be applied to DSMC 2-D axisymmetric simulations. To study the impact of thermal and chemical ablation, we discuss and compare the simulation results among nonreacting, reacting, reacting thermal ablation, and reacting thermal and chemical ablation flow results. Although the importance of modeling chemical reactions for reentry is well documented, the emphasis of previous modeling has been for conditions at peak heating in the continuum region. Because the conditions discussed here are for transitional flows, less is known about the sensitivity of these results to chemical models. The altitude impact on the ablation flow will be further discussed by comparing the flow and surface results at 81 and 68.9 km. The DSMC numerical parameters for the forebody and

wake flow calculations are summarized in Table 5 for the Stardust reacting thermal and chemical ablation simulations at 68.9 and 81 km. Note that one cell can be divided up to 50 subcells based on local mean free path. The number of cells and subcells is chosen so that the collision grid size is on the order of the local mean free path, and the simulation results are independent of the number of grids.

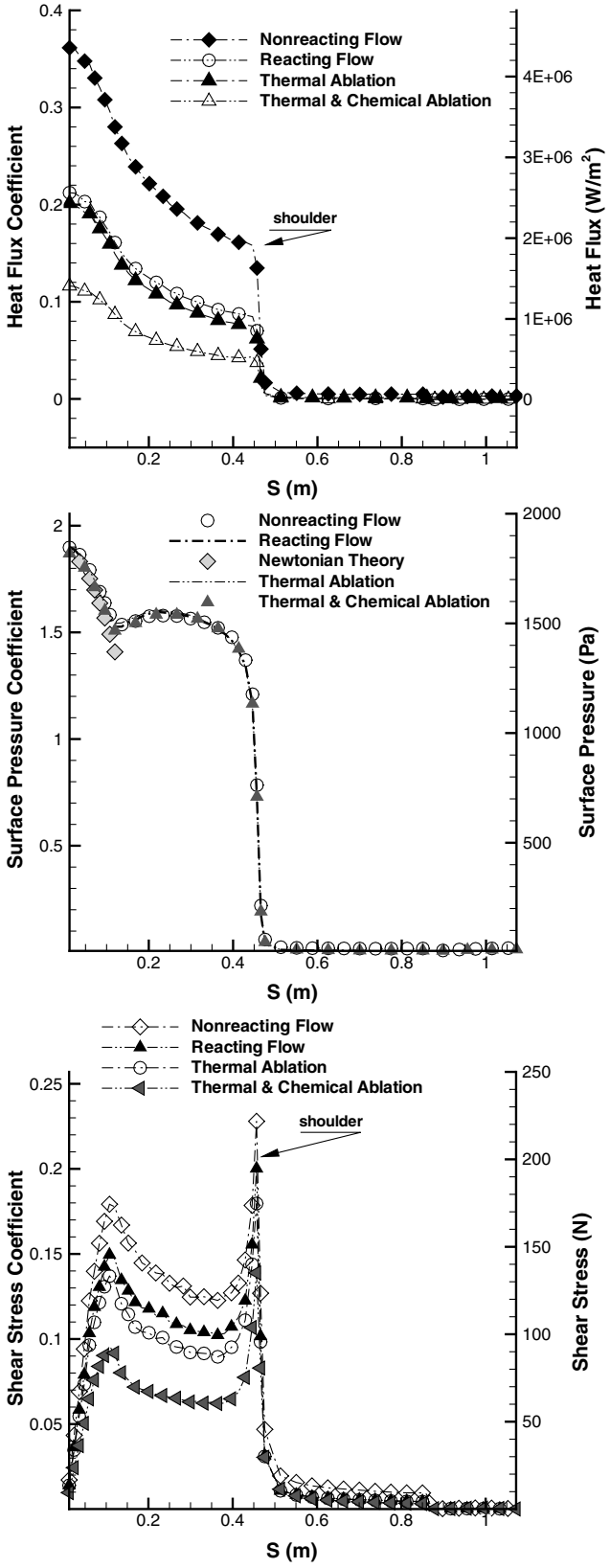

Fig. 6 Stardust heat flux, surface pressure, and shear stress for nonreacting, reacting, reacting thermal ablation, and reacting thermal and chemical ablation flows at 81 km.

The variable hard sphere (VHS) collision model was used and the parameters were obtained from high-temperature viscosity data up to 15,000 K, because no data were available at higher temperatures [13]. Therefore, high-temperature viscosity data are extended and used in this work for the Stardust simulations. The comparison between neutral and ionized flow will be shown and the impact of ionization processes will be further discussed.

A. Forebody Region Flowfield

Figure 7 compares gas number density, axial velocity, pressure, and gas translational temperatures along the stagnation line among the four modeling cases. As shown in Fig. 7, there are small differences between the reacting and nonreacting flows, and the impact of thermal and chemical ablation on these flow macroparameters is not significant along the forebody stagnation line. It can be seen that the gas number density in the reacting flow is higher than its value in the nonreacting flow due to the molecular dissociation process. Because the dissociation process removes energy from the flow, the reacting flow translational temperature is significantly lower than the nonreacting flow temperatures. Compared with the nonreacting flow, the reacting flow gas pressure is quite close to the nonreacting flow value due to the countereffects in the increase of the number density and decrease of the temperature in the reacting flow.

Figure 8 shows species number density along the forebody stagnation line for the chemical reacting flow with and without ablation. Because the ablation reactions do not change the N_2 and O_2 concentrations in the chemically reacting flow, the two curves of N_2 and O_2 are not shown in the two bottom portions of Fig. 8. At the forebody stagnation point, the N_2 number density in the reacting flow is about 30 times less than its value in the nonreacting flow, whereas the O_2 number density is about 3 orders of magnitude less. Most of the N_2 and O_2 molecules dissociate to form atomic N and O atoms through the shock region causing the N and O atoms to be the dominant species in the region close to the forebody stagnation point. For the case of reacting thermal ablation, Fig. 8 shows that as the C and CO species are released into the flow from the forebody surface during thermal ablation, the concentration of C atoms in the forebody stagnation region is higher than N_2, O_2, and NO molecules, although it is still about 1 order of magnitude less than the N and O atoms. The concentration of CO, as shown in the bottom left figure of Fig. 8, is about 1 order of magnitude less than the C species produced by the CO dissociation process in the forebody stagnation region. It can be seen that the atomic C species can diffuse upstream from the stagnation point to a longer distance than the CO molecules because the lighter C atom has a higher diffusion speed than the heavier CO molecule.

The impact of chemical ablation, as shown in the bottom right portion of Fig. 8, is significant compared with thermal ablation, as shown in the bottom left plot of Fig. 8. The concentrations of N and O atoms increase at locations close to the stagnation point for the flow without chemical ablation. However the chemical ablation process consumes a large amount of atomic N and O close to the wall and simultaneously releases CO and CN molecules back into the flow. This process, as shown in the bottom right figure, causes the N and O number density close to the wall to decrease, while significantly increasing the CO and CN number density. It can be seen from the

Table 5 The DSMC simulation parameters for Stardust flows at 68.9 and 81. km; F_{num} refers to the number of real particles represented by one simulated particle

	68.9 km	81 km
Computational domain, m	1.5×1.0	1.5×1.0
Number of cells	375×250	300×200
Subcells per cell	50	50
Time step, s	8.0×10^{-8}	1.0×10^{-7}
F_{num}	$5.0 \times 10^{+12}$	$2.0 \times 10^{+12}$
Total particles	$9.8 \times 10^{+6}$	$5.4 \times 10^{+6}$
Sampled time steps	120,000	80,000

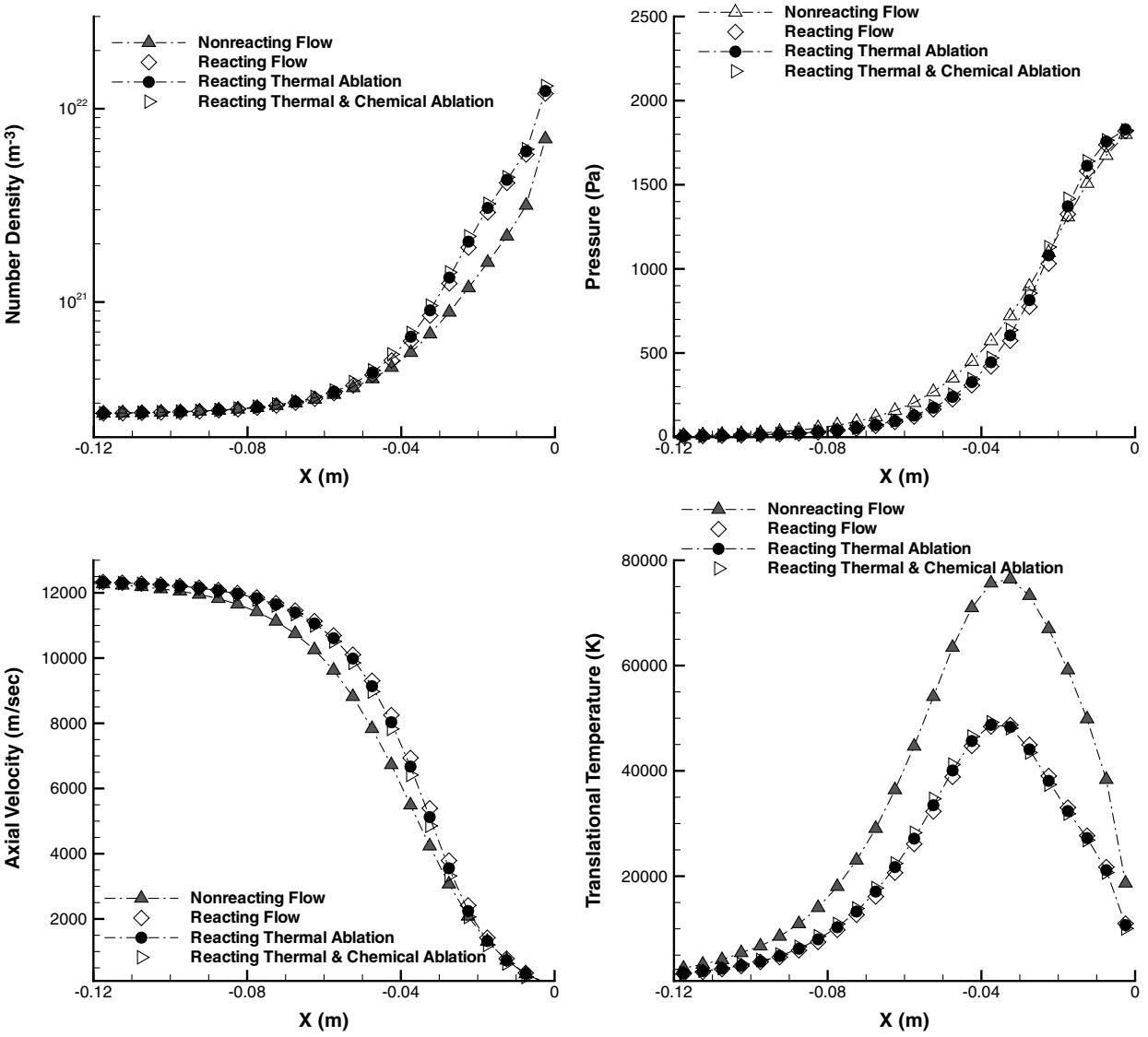

Fig. 7 Comparison of gas number density, pressure, axial velocity, and translational temperature along the forebody stagnation line for the nonreacting, reacting, reacting thermal ablation, and reacting thermal and chemical ablation flows at 81 km.

bottom right figure of Fig. 8, for chemical ablation the dominant species close to the wall are N, O, CO, CN, and C in the flow. Again, the CN and CO number densities decrease rapidly as the flow moves upstream due to a smaller diffusion speed, compared with the C atom. The simulation results indicate that the chemical ablation rates of CO and CN are approximately 5.0×10^{-2} and 8.16×10^{-2} kg/m^2/s, respectively, at the forebody stagnation point.

B. Afterbody Region Flowfield

Figure 9 compares the afterbody gas number density, pressure, axial velocity, and translational temperature along the afterbody centerline for nonreacting, reacting, thermal ablation, and thermal and chemical ablation flows. As expected, the inclusion of chemical reactions in the flow has significant impact on the afterbody gas macroparameters of number density and temperature. The difference in gas pressure between simulations with and without chemical reactions increases in the afterbody region, as compared in the forebody region. Figure 9 also shows that thermal ablation has no observable impact on the afterbody gas macroparameter parameters, as was found in the forebody region. However, the inclusion of chemical ablation in the flow modeling increases the gas number density and pressure about a factor of two in the region close to the afterbody, and significantly decreases the gas axial velocity and temperature in the wake.

Figure 10 shows the gas number density for different chemical species along the afterbody centerline for nonreacting, reacting, thermal ablation, and thermal and chemical ablation flows. The composition of the wake flow primarily originates from the diffusion of species present in the bow shock. Because most of N_2 and O_2 molecules dissociate into atomic N and O atoms in the forebody shock region, as shown in Fig. 8, the atomic N and O number density in the reacting wake region is more than 2–3 orders of magnitude greater than that for N_2 and O_2 molecules. Note that the NO molecule is not observed in the wake due to a high dissociation rate in the forebody region. Therefore, atomic N and O are the main species in the reacting waking flow, compared with the nonreacting flow where the N_2 and O_2 molecules are the main species, as shown in the two top figures of Fig. 10.

The thermal ablation products of C, CO, and CN species are found in the afterbody region as shown in the bottom left figure of Fig. 10. Compared with the case of reacting flow with no surface ablation, there is no significant change of the N and O number density in the wake region. Note that thermal ablation products are initially generated in the forebody region because the afterbody surface heat flux is almost zero, as discussed earlier. Because the atomic C has a higher number density in the forebody region, and a higher diffusion speed compared with the molecular CO and CN, it also has a higher

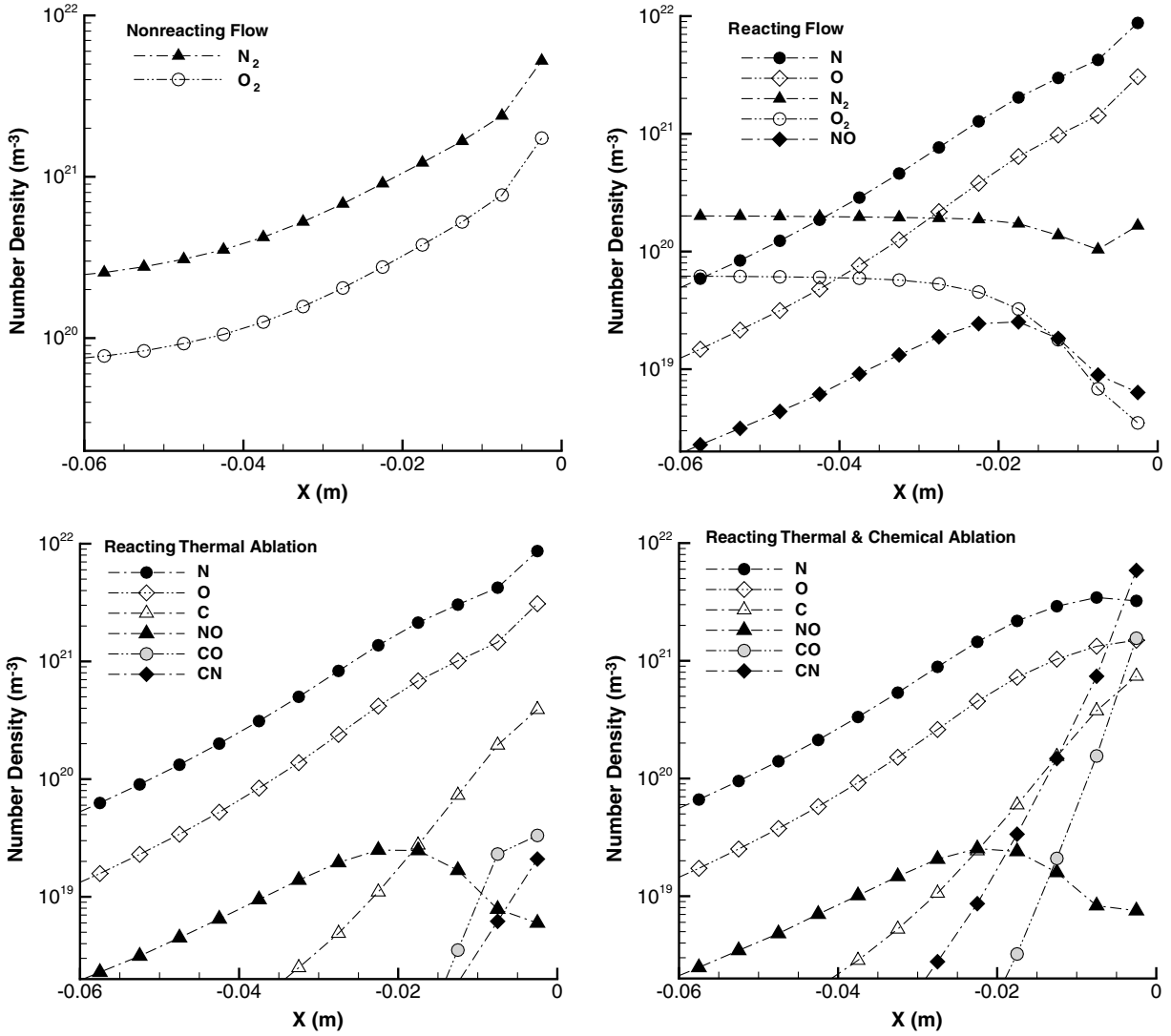

Fig. 8 Comparison of species number densities along the forebody stagnation line for nonreacting, reacting, reacting thermal ablation, and reacting thermal and chemical ablation flows at 81 km.

concentration in the afterbody region. In the chemical ablation flow, as shown in the bottom right figure of Fig. 10, the atomic O and N are significantly consumed due to the gas–wall reactions in the region close to the wall. The importance of gas–wall reactions causes the amount of CO and CN molecules in the chemical ablation flow to be about an order of magnitude larger than their concentrations in the thermal ablation flow, although the N and O number densities decrease in the afterbody region. Note that the concentration of the ablation products, C, CO, and CN, are almost constant along the afterbody centerline because the diffusion direction, from the higher to lower concentration region, is toward the downstream. This is in contrast to the forebody region where the ablation products diffuse upstream.

Finally, as discussed in Sec. III, it can be seen from the results presented in the last two sections that the CN radical concentration, for any of the ablation models, is orders of magnitude higher than that obtained from the shock heated dissociation CO_2 in air. This result is in general agreement with the Stardust observations.

C. Sensitivity to Altitude

The different freestream conditions at various altitudes may not only impact the reentry vehicle surface parameters and reacting flowfield, but also the ablation flow as discussed in this work. To study the impact of altitude, we compare the ablation flow results at 81 and 68.9 km. Note that the Stardust forebody thermal ablation rate increases from 0.016 at 81 km to 0.04 kg/(m^2 s) (60% C and 40% CO) at 68.9 km, as modeled by Olynick et al.[8]. Figure 11 compares the Stardust heat flux and surface temperatures for reacting thermal and chemical ablation flow at 81 and 68.9 km. It is well known that as the altitude decreases, the flow becomes denser and the shock becomes stronger. The denser shock at 68.9 km causes a significant increase of the forebody heat flux and surface temperature, although the forebody heat transfer coefficients decrease. At these two altitudes, the afterbody surface heat flux and temperatures are quite close and are much less than the forebody surface values. However, the denser flow at lower altitudes creates a smaller expansion angle at the shoulder position, leading to a larger recirculation region, as shown in Fig. 12. The formation mechanism of an aft vortex as well as the vortex size behind a slender or blunt body has been discussed in detail in [14]. The vortex size sensitivity to freestream density for the Stardust wake region is consistent with our previous results. In the previous work [14], the normalized vortex size defined as the ratio of the wake recirculation length to the base radius was approximately 1.28 at an altitude of 80 km, greater than the normalized vortex size value of approximately unity at the altitude of 81 km shown in Fig. 12. This is because in this work the gas-expansion angle at the base shoulder location ($x = 0.557$ m and $y = 0.19$ m of Fig. 1) is larger than the value calculated in the previous work, which greatly reduces the recirculation space in the wake region.

Figure 13 compares the Stardust reacting thermal and chemical ablation product number density along the forebody and afterbody centerline at 81 and 68.9 km. It can be seen that the concentrations of the ablation products, C, CO, and CN, are higher at 68.9 km than at

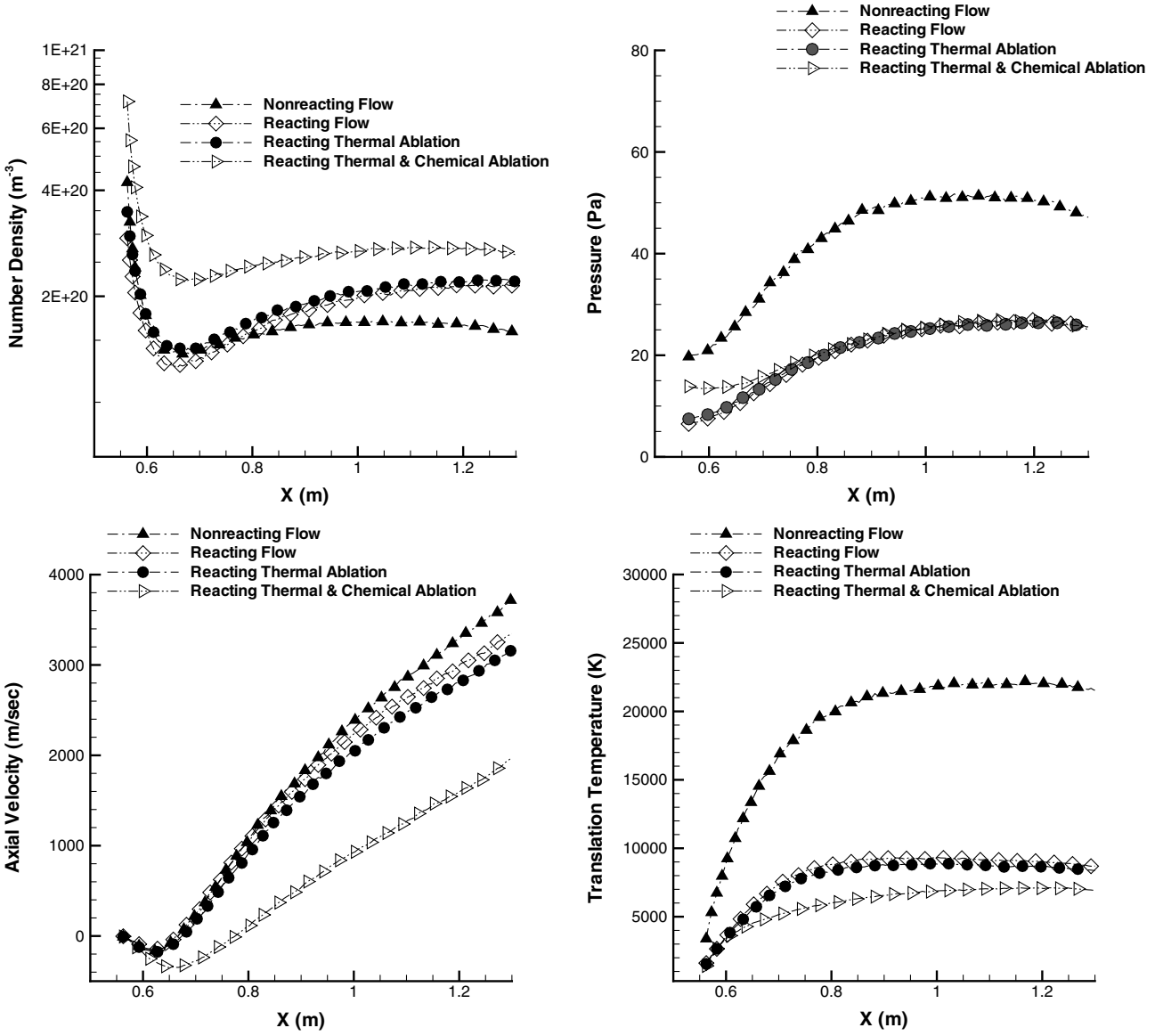

Fig. 9 Afterbody gas number density, pressure, axial velocity, and translational temperature along the centerline for nonreacting, reacting, reacting thermal ablation, and reacting thermal and chemical ablation flows at 81 km.

81 km in the region close to the forebody stagnation point and the afterbody region. The surface thermal ablation rate is higher at 68.9 km due to higher surface heat flux and temperature, and the chemical ablation rate is also higher at 68.9 km due to higher concentrations of N and O atoms in the flow and higher oxidation rates. Because it is more difficult for the ablation products at 68.9 km to diffuse upstream through a denser gas environment, the number densities decrease more rapidly along the forebody stagnation line compared with 81 km. However, in the afterbody region, the higher ablation rate always generates higher concentrations of ablation products because the diffusion direction is the same as the flow direction.

D. Neutral and Ionized Flows

In this subsection, we investigate the surface material ablation effect on the ionization flow. It is well known that ultrahigh Mach number reentry vehicles create sufficient energy causing substantial ionization in the forebody shock region. Recently, Ozawa et al. [13] developed kinetic-based energy models to simulate hypersonic ionization flow. In this work, we will apply the same DSMC ionization modeling techniques as described in [13], which can be briefly described as follows. Charge neutrality is assumed because the Debye length is much less than the local mean free path, and to maintain charge neutrality electrons are moved in the DSMC simulation based on the local averaged ion velocity. The variable hard sphere model was corrected to use high-temperature viscosity data, and new vibration-translation collision numbers were developed to model electron-impact molecular-excitation processes [13]. The ionization processes listed in Table 4 are included in this work.

Figure 14 shows the distributions of total, ion, and electron number densities along the stagnation line at 81 km with charged species. It can be seen that exact charge neutrality is obtained, and the maximum degree of ionization, defined as the ratio of electron or ion number density to the total number density, along the stagnation line is seen to be approximately 3% at this altitude of 81 km. Ablation processes reduce the degree of ionization by about 1 to 2% compared with earlier results shown in [13] of 5%. This is because the ablation process consumes atomic N and O molecules, which are the sources of the ionization processes. Distributions of charged species N^+, O^+, N_2^+, O_2^+, and NO^+ number densities along the stagnation line are shown in Fig. 15. Far from the body, N_2^+ is the main ionic species, but near the body, due to electron impact ionization reactions, the N^+ and O^+ concentrations are significantly increased and N^+ becomes the dominant ionic species. The number density of diatomic ion species are decreased near the body because the recombination rates in the flowfield and on the surface are higher than the production rates. The

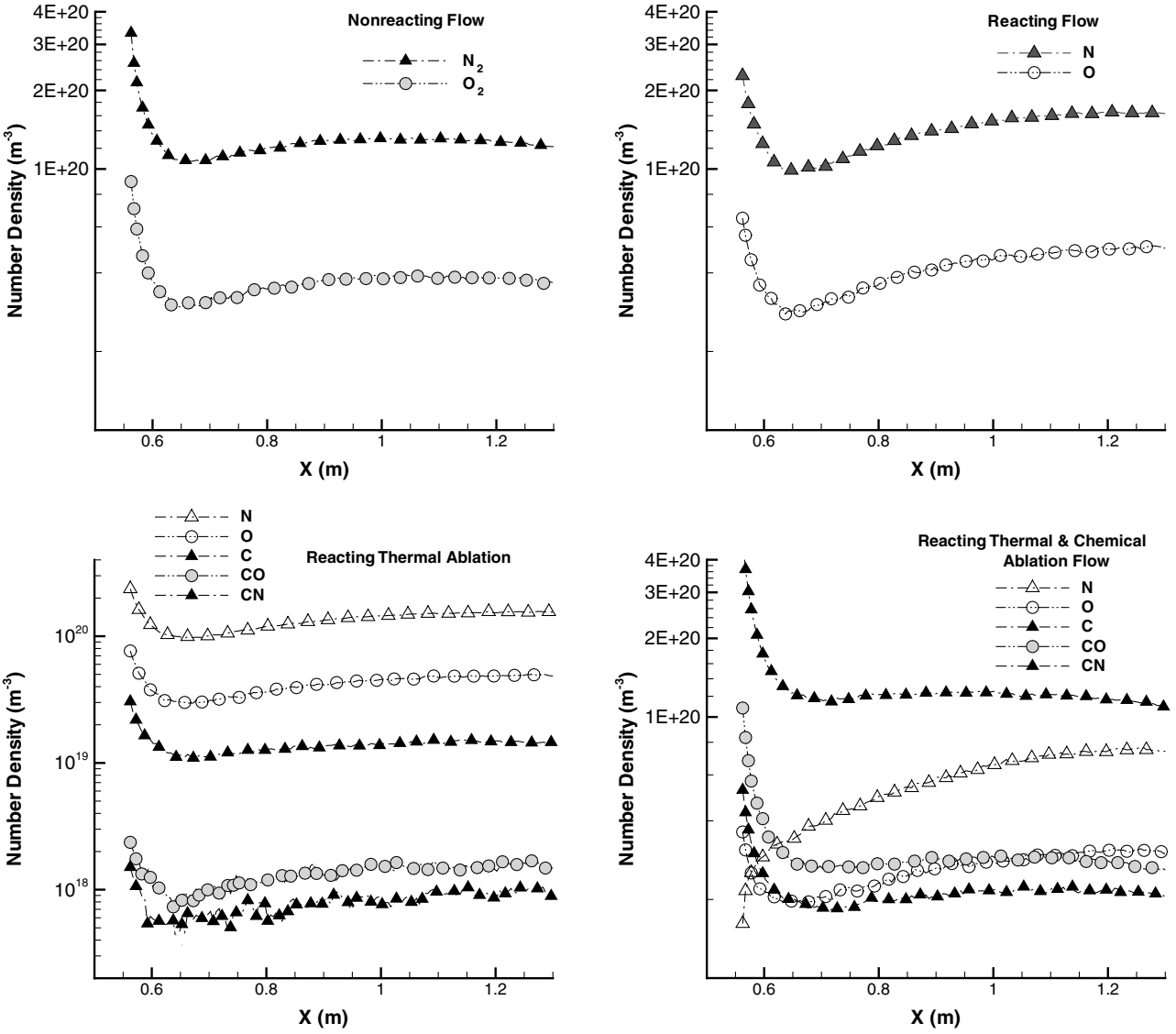

Fig. 10 Afterbody gas species number densities along the centerline for nonreacting, reacting, reacting thermal ablation, and reacting thermal and chemical ablation flows at 81 km.

relative concentration of ions produced in the shock is $N^+ > N_2^+ > O^+ > NO^+ > O_2^+$ at 81 km. However, as shown in Fig. 16, the dominant ionic species in the wake region are N^+ and O^+, and the concentration of ionic species is more than 3 orders of magnitude less than the neutral species. This is because the ionization processes mainly occur in the forebody shock region, and the lighter N^+ and O^+ ionic species convect more easily back to the wake region than the heavier ionic species.

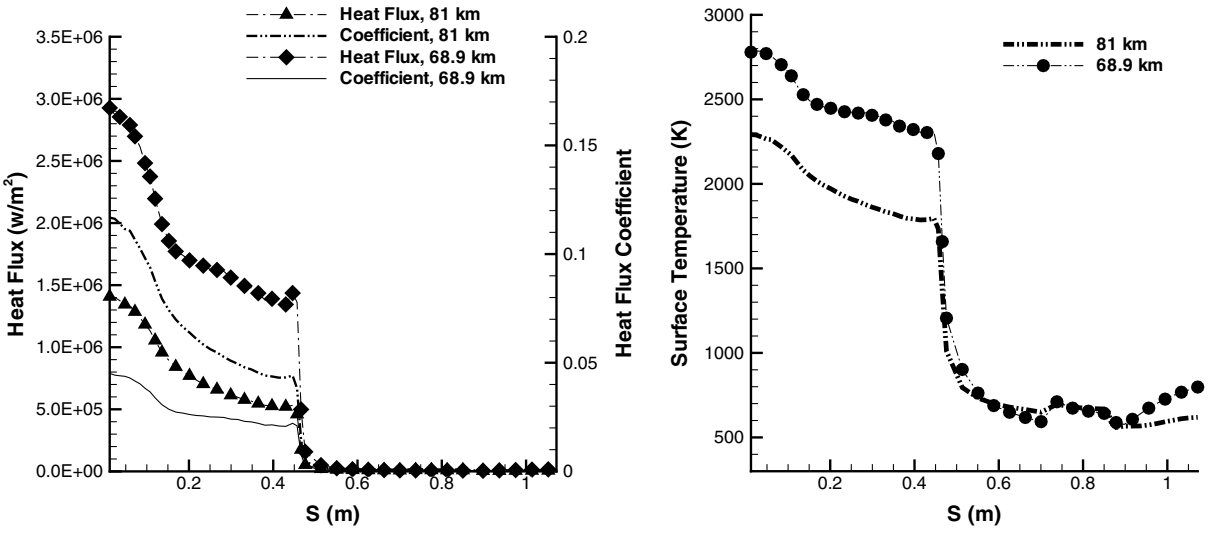

Fig. 11 Comparison of Stardust surface heat flux and temperature for reacting thermal and chemical ablation flow at 81 and 68.9 km.

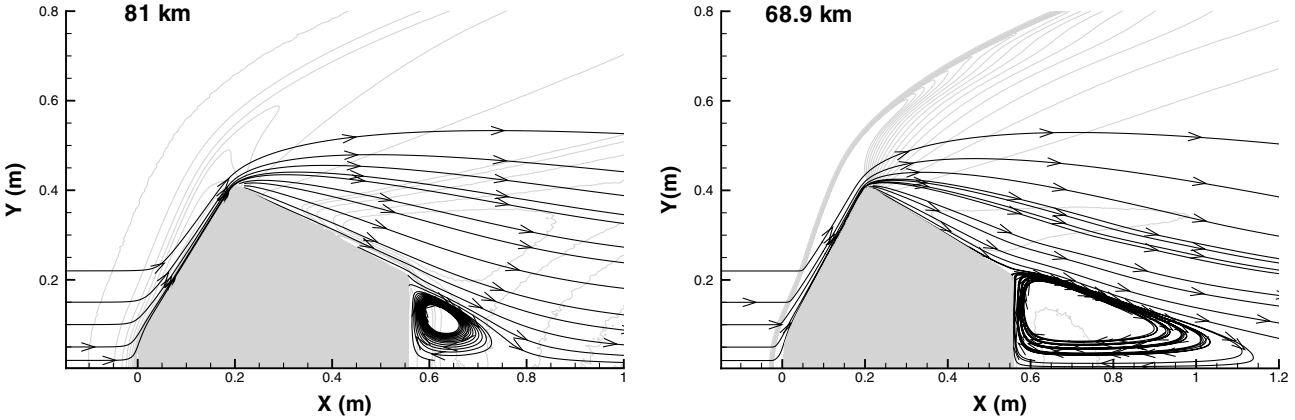

Fig. 12 Comparison of Stardust afterbody recirculation size for reacting thermal and chemical ablation flow at 81 and 68.9 km.

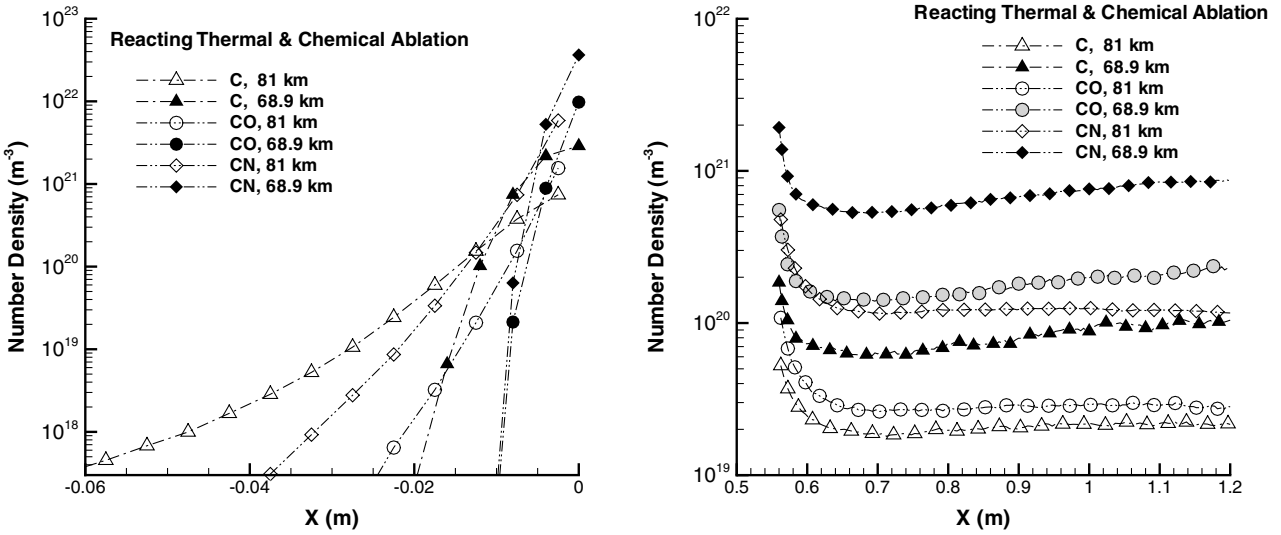

Fig. 13 Comparison of Stardust ablation product number density along the forebody (left) and afterbody (right) centerline at 81 and 68.9 km.

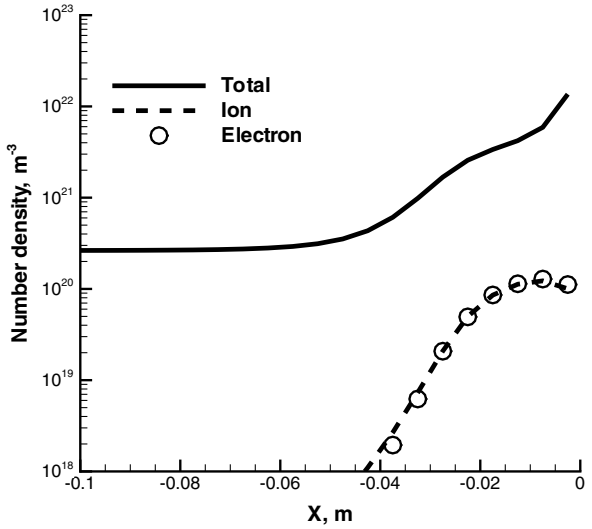

Fig. 14 Distributions of total, ion, and electron number densities along the stagnation line for the Stardust blunt body at 81-km altitude for freestream velocity of 12.4 km/s with charged species.

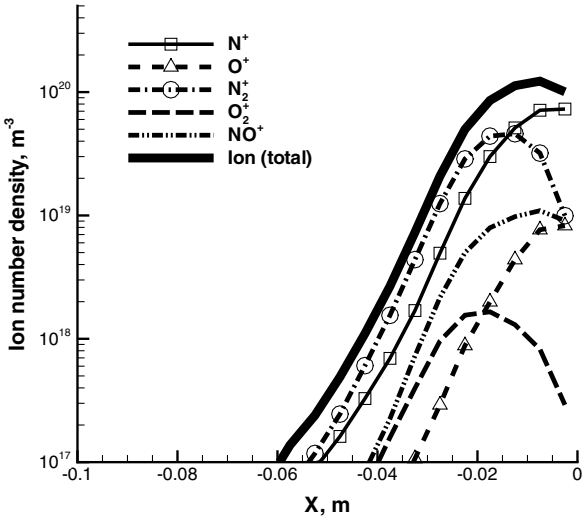

Fig. 15 Distributions of N^+, O^+, N_2^+, O_2^+, and NO^+ number densities along the stagnation line for the Stardust blunt body at 81-km altitude for freestream velocity of 12.4 km/s with charged species.

Accurate prediction of the distribution of electron number density is critical to the calculation of the plasma frequency f_p (Hz), where

$$f_p = \frac{1}{2\pi}\left(\frac{e^2 n_e}{\epsilon_0 m_e}\right)^{1/2}, \qquad \approx 8.98\sqrt{n_e} \quad (\mathrm{m}^{-3}) \tag{8}$$

which is further used to determine the communication blackout based on the critical electron number density $n_{e,\mathrm{critical}}$. For X-band (such as $f = 8.4$ GHz), [12] assesses a value of $n_{e,\mathrm{critical}}$ of approximately 8.75×10^{17} m^{-3}. It has been predicted for the Stardust reentry flow at 81 km that electron number density in the forebody stagnation region is about 2.0×10^{20} m^{-3} and about $1.0 \times$

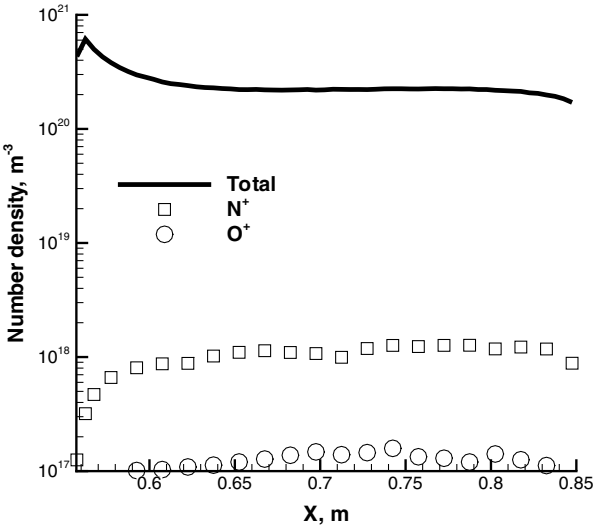

Fig. 16 Distributions of total, N^+, and O^+ number densities along the wake stagnation line for the Stardust blunt body at 81-km altitude for freestream velocity of 12.4 km/s with charged species.

10^{18} m^{-3} in the wake region. Because these values are greater than the critical value, communication blackout [37] is predicted, which is consistent with the available blackout studies in the literature. For the Mars Science Lab (MSL) [38] with a velocity of 7.4 km/s at 56 km, it was predicted that the electron number density is about 1.2×10^{20} m^{-3} in the forebody region and about 1.1×10^{18} m^{-3} in the wake region. For the Apollo [39] reentry with a velocity of 9.5 km/s at 75 km, it was predicted that the electron number density is about 2.86×10^{20} and 2.0×10^{18} m^{-3} in the forebody and wake region. Communication blackout was predicted for these cases, as well as the RAM-C II and space shuttle reentry cases [40]. It can be seen that our predicted electron number density in both forebody shock and afterbody wake regions are of a reasonable magnitude, consistent with the preceding published results. It is also critical to include surface ablation effects to accurately predict electron distribution for the Stardust reentry process and to further predict communication blackout frequency.

VII. Conclusions

The direct simulation Monte Carlo method has been applied in this work to study the Stardust ionized, reacting, thermal, and chemical ablation flows at 68.9 and 81 km. The purpose of this work is to study the impact of the surface thermal protection layer ablation process on surface properties, the flowfield, and communications blackouts.

An iterative method has been applied to obtain an accurate surface temperature distribution based on a thermal equilibrium condition between convective heating and body radiation cooling. The DSMC simulation predictions of the surface properties and flowfield are compared for nonreacting, reacting, reacting thermal ablation, and reacting thermal and chemical ablation flows. It was found that thermal ablation has limited impact compared with the chemical ablation for these high-altitude conditions. This is because the thermal ablation rate is quite small, and only contributes on the forebody surface. The chemical ablation process significantly decreases the forebody surface heat flux, approximately from 240 to 120 W/cm^2 at the forebody stagnation point. Thus, the chemical ablation is an effective cooling procedure for these transitional conditions. Chemical ablation also greatly impacts the species distribution in the flowfield. It has been shown that chemical ablation significantly decreases the N and O number density, although it increases the CO and CN number density in the region close to the forebody. In the afterbody region, the chemical ablation product CN becomes a dominant species because the ablation products diffuse towards the downstream. As the altitude decreases, the impact of reacting thermal and chemical ablation on the flowfield increases due to a denser freestream flow.

The effect of ionization processes has also been investigated for the communication blackout. The predicted electron number densities in the forebody bow shock and afterbody wake region and the concentration are compared with the similar reentry cases available in the literature, and good agreement has been achieved. In this work, it was found that ablation causes a decrease in the degree of ionization because it consumes atomic N and O species in the flow, which are important ionization sources. Therefore, accurate modeling of surface ablation is critical to predict electron number density and blackout frequency. Finally, communication blackout is predicted for a Stardust-like reentry trajectory at 81 km at an *X*-band frequency ($f = 8.4$ GHz).

Modeling of high-speed, high-temperature reentry chemical reaction, ionization, and ablation flow is challenging, and there are potential problems with the presented physical models, which may impact the simulation results. First, because the gas temperature for Stardust reentry is above 50,000 K, the fidelity of the chemical and ionization reaction rates, as well as VHS model temperature exponents needs to be further validated in this high-temperature region. Second, because the VHS model distributes the post-collision relative velocity equally in all directions, the accuracy of VHS to diffusion dominant wake flow need to be further studied. Third, the contribution of the radiative heat flux to the chemically reactive flowfield was not considered in this work, and may be important for the lower-altitude case.

Acknowledgments

The research performed at Pennsylvania State University was supported by NASA Ames Research Center through the Eloret agreement no. 85224 entitled "Stardust Post-Flight Data Analysis" and NASA grant and cooperative agreement no. NNX07AC47A, whose support is gratefully acknowledged. Special thanks are to M. Ivanov of the Institute of Theoretical and Applied Mechanics, Russia, for the use of the original SMILE code, and to J. N. Moss for providing DS2V simulation results for comparison and helpful discussions.

References

[1] Covington, M. A., Heinemann, J. M., and Goldstein, H. E., "Performance of a Low Density Ablative Heat Shield Material," AIAA Paper 2004-2273, Portland, OR, June 2004.

[2] Gosse, R., and Candler, G., "Ablation Modeling of Electro-Magnetic Launched Projectile for Access to Space," AIAA Paper 2007-1210, Reno, NV, Jan. 2007.

[3] Suzuki, T., Furudate, M., and Sawada, K., "Unified Calculation of Hypersonic Flowfield for a Reentry Vehicle," *Journal of Thermophysics and Heat Transfer*, Vol. 16, No. 1, 2002, pp. 94–100.

[4] Palaninathan, R., and Bindu, S., "Modeling of Mechanical Ablation in Thermal Protection System," *Journal of Spacecraft and Rockets*, Vol. 42, No. 6, 2005, pp. 971–979. doi:10.2514/1.10710

[5] Chen, Y.-K., and Milos, F. S., "Navier–Stokes Solutions with Finite Rate Ablation for Planetary Mission Earth Reentries," *Journal of Spacecraft and Rockets*, Vol. 42, No. 6, 2005, pp. 961–970. doi:10.2514/1.12248

[6] Jenniskens, P., "Observation of the Stardust Sample Return Capsule Entry with a Slit-Less Echelle Spectrograph," AIAA Paper 2008-1210, Jan. 2008.

[7] Wilmoth, R. G., Mitcheltree, R. A., and Moss, J. N., "Low-Density Aerodynamics of the Stardust Sample Return Capsule," *Journal of Spacecraft and Rockets*, Vol. 36, No. 3, 1999, pp. 436–441.

[8] Olynick, D., Chen, Y.-K., and Tauber, M. E., "Aerothermodynamics of the Stardust Sample Return Capsule," *Journal of Spacecraft and Rockets*, Vol. 36, No. 3, 1999, pp. 442–462.

[9] Gupta, R. N., "Aerothermodynamic Analysis of Stardust Sample Return Capsule with Coupled Radiation and Ablation," *Journal of Spacecraft and Rockets*, Vol. 37, No. 4, 2000, pp. 507–514.

[10] Starkey, R. P., "Electromagnetic Wave/Magnetoactive Plasma Sheath Interaction for Hypersonic Vehicle Telemetry Blackout Analysis," AIAA Paper 2003-4167, June 2003.

[11] Mather, D. E., Pasqual, J. M., and Sillence, J. P., "Radio Frequency (RF) Blackout During Hypersonic Reentry," AIAA Paper 2005-3443, May 2005.

[12] Morabito, D. D., "The Spacecraft Communications Blackout Problem Encountered During Passage or Entry of Planetary Atmospheres," NASA Jet Propulsion Lab., Rept. IPN PR 42-150, Los Angeles, Aug. 2002.

[13] Ozawa, T., Zhong, J., and Levin, D. A., "Development of Kinetic-based Energy Exchange Models for Transitional, Ionized Hypersonic Flows," *Physics of Fluids* (to be published).

[14] Zhong, J., Ozawa, T., and Levin, D. A., "Comparison of High-Altitude Hypersonic Wake Flows of Slender and Blunt Bodies," *AIAA Journal*, Vol. 46, No. 1, 2008, pp. 251–262. doi:10.2514/1.31056

[15] Ivanov, M. S., Markelov, G. N., and Gimelshein, S. F., "Statistical Simulation of Reactive Rarefied Flows: Numerical Approach and Applications," AIAA Paper 1998-2669, June 1998.

[16] Gimelshein, S. F., Levin, D. A., and Collins, R. J., "Modeling of Glow Radiation in the Rarefied Flow About an Orbiting Spacecraft," *Journal of Thermophysics and Heat Transfer*, Vol. 14, No. 4, 2000, pp. 471–479.

[17] Bose, D., Michael, M. J., Bogdanoff, D. W., Raiche, G. A., and Allen, G. A., "Modeling and Experimental Assessment of CN Radiation Behind a Strong Shock Wave," *Journal of Thermophysics and Heat Transfer*, Vol. 20, No. 2, 2006, pp. 220–230.

[18] Whiting, E. E., Arnold, J. O., Page, W. A., and Reynolds, R. M., "Composition of the Earth's Atmosphere by Shock-Layer Radiometry During the PAET Entry Probe Experiment," *Journal of Quantitative Spectroscopy and Radiative Transfer*, Vol. 13, No. 9, 1973, pp. 837–859. doi:10.1016/0022-4073(73)90125-8

[19] Park, C., Howe, J. T., Jaffe, R. L., and Candler, G. V., "Review of Chemical-Kinetic Problems of Future NASA Missions, 2: Mars Entries," *Journal of Thermophysics and Heat Transfer*, Vol. 8, No. 1, 1994, pp. 9–23. doi:10.2514/3.496

[20] Bird, G. A., *Molecular Gas Dynamics and the Direct Simulation of Gas Flows*, Clarendon, Oxford, England, U. K., 1994.

[21] Bird, G. A., "Monte-Carlo Simulation in an Engineering Context," *Rarefied Gas Dynamics*, edited by S. Fisher, Vol. 74, AIAA New York, 1981, pp. 239–255.

[22] Park, C., *Nonequilibrium Hypersonic Aerothermodynamics*, Wiley, New York, 1990.

[23] Gordon, S., and McBride, B. J., "Computer Program for Calculation of Complex Chemical Equilibrium Compositions and Applications," NASA RP-1311, Oct. 1994.

[24] Boyd, I. D., "Monte Carlo Simulation of Nonequilibrium Flow in a Low-Power Hydrogen Arcjet," *Physics of Fluids*, Vol. 9, No. 10, 1997, pp. 3086–3095. doi:10.1063/1.869474

[25] Ivanov, M. S., and Rogasinsky, S. V., "Analysis of the Numerical Techniques of the Direct Simulation Monte Carlo Method in the Rarefied Gas Dynamics," *Soviet Journal of Numerical Analysis and Mathematical Modelling*, Vol. 3, No. 6, 1988, pp. 453–465.

[26] Moss, J. N., Glass, C. E., and Greene, F. A., "DSMC Simulations of Apollo Capsule Aerodynamics for Hypersonic Rarefied Conditions," AIAA Paper 2006-3577, June 2006.

[27] Doihara, R., and Nishida, M., "Ablation Studies for a Super-Obital Reentry Capsule Using a Three-Temperature Model," *Transactions of the Japan Society for Aeronautical and Space Sciences*, Vol. 47, No. 157, 2004, pp. 161–166. doi:10.2322/tjsass.47.161

[28] Wright, M., Loomis, M., and Papadopoulos, P., "Aerothermal Analysis of the Project Fire II Afterbody Flow," *Journal of Thermophysics and Heat Transfer*, Vol. 17, No. 2, 2003, pp. 240–249.

[29] Tran, H., Johnson, C. E., Rasky, D. J., Hui, F. C., Hsu, M.-T., Chen, T., Chen, Y.-K., Paragas, D., and Kobayashi, L., "Phenolic Impregnated Carbon Ablators (PICA) as Thermal Protection Systems for Discovery Missions," NASA TM-110440, Apr. 1997.

[30] Zhong, J., Ozawa, T., and Levin, D. A., "Modeling of Stardust Reentry Reacting Thermal and Chemical Ablation Flow," 39th AIAA Thermophysics Conference, AIAA Paper 2007-4551, June 2007.

[31] Moss, J., Glass, C., and Greene, F., "DSMC Simulations of Apollo Capsule Aerodynamics for Hypersonic Rarefied Conditions," AIAA Paper 2006-3577, June 2006.

[32] Sutton, K., "Air Radiation Revisited," AIAA Paper 1984-1733, June 1984.

[33] Sutton, K., and Grave, R. A., Jr., "A General Stagnation Point Convective Heating Equation for Arbitrary Gas Mixtures," NASA Langley Research Center Report TR R-376, Hampton, VA, Nov. 1971.

[34] Herdrich, G., Auweter-Kurtz, M., Bohrk, H., Fertig, M., and Lohle, S., "Test Facilities for High Enthalpy Planetary Entry Simulation," 5th European Workshop on Thermal Protection Systems and Hot Structures, Noordwijk, The Netherlands, AIAA Paper 2006-1712, 2006.

[35] Tauber, M. E., and Meneses, G. P., "Aerodynamics of Transatmospheric Vehicles," AIAA Paper 1986-1257, June 1986.

[36] Anderson, J. D., *Hypersonic and High-Temperature Gas Dynamics*, 2nd ed., AIAA, Reston, VA, 2006.

[37] Mather, D. E., Pasqual, J. M., and Sillence, J. P., "Radio Frequency (RF) Blackout During Hypersonic Reentry," AIAA Paper 2005-3443, May 2005.

[38] Morabito, D., and Edquist, K., "Communications Blackout Predictions for Atmospheric Entry of Mars Science Laboratory," Inst. of Electrical and Electronics Engineers Paper 2005-1163, Mar. 2005.

[39] Morabito, D. D., "The Spacecraft Communications Blackout Problem Encountered During Passage or Entry of Planetary Atmospheres," NASA Jet Propulsion Lab. Rept. IPN PR 42-15, Los Angeles, Aug. 2002.

[40] Starkey, R. P., "Electromagnetic Wave/Magnetoactive Plasma Sheath Interaction for Hypersonic Vehicle Telemetry Blackout Analysis," AIAA Paper 2003-4167, June 2003.

C. Kaplan
Associate Editor